Eng. Sci., 2025, **36**, 1636

Engineered Science
DOI: https://dx.doi.org/10.30919/es1636

Aerogels of Cellulose Nanofibers@Metal-Organic Frameworks for Carbon Dioxide Capture

Yong Sha,[1] Shuliang Li,[2,*] Xuefeng Li,[1] Miao He,[1] Yihui Wu,[1] Yunrui Gao,[2] Junjia Hu[2] and Xianmin Mai [2,*]

Abstract

In this study, three carboxylic acid-functionalized metal-organic framework (MOF) materials (UiO-66, UiO-66-COOH, and UiO-66-2COOH) were synthesized using renewable cellulose aerogel (CA). A composite adsorbent (UiO-66-X/CA), characterized by a high specific surface area, abundant active sites, and excellent structural stability, was successfully developed. Under the conditions of 273K and $P/P_0 = 0.1$, GCMC simulations show that in the UiO-66 series of materials, an increase in the number of carboxylic acid modifications leads to an increase in CO_2 adsorption capacity, as well as an increase in the types and strengths of interaction forces. The regulatory mechanism of functional groups on CO_2 adsorption performance was systematically investigated. The incorporation of carboxylic acid groups significantly enhanced the CO_2 affinity of the composite material. The study investigated the loading amounts of three different MOFs and found that a 100% loading ratio exhibited the optimal CO_2 adsorption performance. At 273K and 1 bar, the CO_2 adsorption capacity of UiO-66-2COOH/CA with 100% loading reached 31.7 cm^3/g, attributed to the synergistic effect of the dicarboxylic acid group. Based on the Ideal Adsorbed Solution Theory (IAST), gas separation performance was predicted according to the flue gas composition (CO_2: N_2 = 15:85). Carboxyl-modified MOFs demonstrated superior selectivity for carbon dioxide adsorption, with a maximum value of 41.9. The breakthrough experiment further proved that UiO-66-COOH/CA exhibited selective adsorption capacity for CO_2/N_2 under both dry and wet conditions. Moreover, the hierarchical pore structure of cellulose aerogel effectively enhanced CO_2 diffusion kinetics. This study elucidates the co-optimization of CO_2 adsorption performance through MOF functionalization and porous carriers, providing a strategy for the development of scalable and bio-based carbon capture materials. Additionally, the integration of cellulose aerogel addressed the processing challenges of MOF powders, offering new insights into the practical application of MOF materials.

Keywords: Metal-organic frame materials; Carboxylic acid functionalization; Cellulose aerogel; Carbon dioxide adsorption.
Received: 09 April 2025; Revised: 13 June 2025; Accepted: 16 July 2025.
Article type: Research article.

1. Introduction

Carbon dioxide is a colorless, odorless gas. The rapid development of industry, the development and utilization of oil, coal and natural gas have led to the emission of a large amount of carbon dioxide gas, and the concentration of carbon dioxide in the atmosphere has increased sharply from 340ppm in 1980 to 426.9ppm in 2024, resulting in environmental damage and greenhouse effect. The continuous intensification of atmospheric greenhouse effect leads to global warming, rising sea level and increasing extreme climate events. To mitigate this problem, China has proposed and implemented a "dual carbon" strategy, emphasizing the need for efficient functional materials to capture and convert carbon dioxide.[1,2] Strategies to convert CO_2 into valuable chemical products not only reduce CO_2 emissions, but also promote the production of carbon-containing chemicals.

Porous materials, such as activated carbon and zeolite molecular sieves, which are traditional adsorbents, exhibit certain limitations in terms of structure, performance, and application. For instance, the specific surface area of activated carbon (ranging from approximately 100 m^2/g to 2000 m^2/g

[1] *School of Chemistry and Environment, Southwest Minzu University, Chengdu, 610041, China*
[2] *School of Architecture, Southwest Minzu University, Chengdu, 610041, China*
* *Email:* lishuliang@swun.edu.cn (S. L. Li), maixianmin@foxmail.com (X. M. Mai)

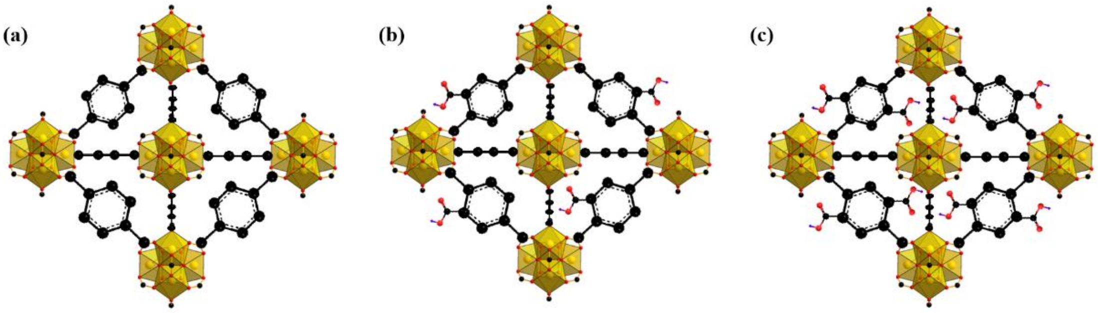

Fig. 1: Structures of (a)UiO-66, (b)UiO-66-COOH, and (c)UiO-66-2COOH.

varies significantly depending on the synthesis method and raw materials, leading to inconsistent adsorption properties.[3] As a physical adsorbent for CO_2, zeolite molecular sieves demonstrate low adsorption capacity under low-pressure conditions and are prone to deactivation in the presence of water.[4]

The ideal adsorption solution theory of pure components (IAST) provides an efficient theoretical prediction tool for CO_2/N_2 selective adsorption, which plays an important role in material screening and process optimization. The selectivity of various zeolites (*e.g.*, 13X, 5A) to CO_2/N_2 was evaluated using IAST. The results show that the selectivity of 13X zeolite to CO_2 at room temperature can reach more than 30, mainly due to its larger pore size and the strong adsorption of cation to CO_2.[5] The selectivity of functionalized MOFs (such as amino-modified UiO-66) to CO_2/N_2 was evaluated by IAST. The results show that the CO_2 selectivity is significantly improved by amino functionalization, especially at low CO_2 concentration (< 0.1 bar), the selectivity can reach more than 50.[6]

As a new type of porous material, Metal organic frameworks (MOF),[1,8,9] are widely used in gas storage,[10,11] separation,[12,13] drug delivery,[14,15] catalysis[16,17] and other aspects.[18,19] MOF's high porosity, [20] prominent specific surface area, [21] adjustable structure, and versatility[22] make it a superior CO_2 adsorbent to many conventional porous adsorbent materials.[23] Most studies in this field focus on: 1. Increasing pore volume and surface area of materials to increase adsorption capacity of materials;[24,25] 2. Groups that have affinity with carbon dioxide are modified on the pore channels to improve adsorption performance.[26-30]

So far, although researchers have conducted extensive research using MOFs to separate gases, the practical application of MOF materials has been limited by their stability, while other MOFs lack thermal stability, hydrothermal stability, and chemical stability, whereas UiO-66 type MOF has thermal stability (up to 813 K) and outstanding water stability. By modifying functional functional groups on the basis of UiO-66, it can produce strong interactions between carbon dioxide molecules, allowing the selective capture of carbon dioxide from different mixtures, and enhancing the force between carbon dioxide and carboxyl by modifying carboxyl groups is a good choice. According to Yang *et al*.,[31] UiO-66-2COOH has excellent trapping performance for carbon dioxide. Through simulation, it is found that CO_2 molecules are mainly distributed in the area near the μ3-OH group and the -COOH organic functional group of $Zr_6O_4(OH)_4$ oxygen cluster nodes. The DES@UiO-66-COOH composite material studied by Zhong *et al*.[32] has a certain absorption of CO_2. DES@UiO-66-COOH (0.05) has a selectivity of 24.7 times that of UiO-66 for CO_2/N_2, which is suitable for selective CO_2 capture in flue gas. It is further indicated that modification of functional carboxyl group is beneficial to enhance the adsorption of carbon dioxide. The powder properties of DES@UiO-66-COOH result in poor processability and difficult molding.

Utilizing their functional design to address environmental pollution challenges, people are increasingly inclined to explore the potential applications of MOFs.[33-35] Owing to the crystalline nature of MOFs, they typically exist in powder form, which poses significant challenges in terms of their machinability and processability.[36-38] In recent years, extensive research has focused on functional group modification and the development of MOF-based composite materials. Dandan Yan *et al*.[39] investigated the effectiveness of MOF-based membranes. Among these, modified MOFs demonstrated the highest efficiency in dye wastewater removal. Asif Hayat *et al*.[40] prepared BC/Mg-MOF-74 with the best decarbonization effect via in-situ growth, where the combination of biochar and Mg-MOF-74 exhibited a synergistic effect on carbon dioxide adsorption.

Currently, research efforts focus on integrating MOFs with structural materials (*e.g.*, graphene, carbon nanotubes, chitosan, cellulose, zeolites) to develop composite materials for practical applications.[41-43] Nanocellulose, particularly in the form of cellulose aerogels, has emerged as a highly promising support material for MOFs due to the advantages of cellulose aerogel nanocrystals, such as high strength, lightweight, non-toxicity, and ease of processing. Therefore, in this study, MOFs were loaded onto aerogels to investigate the CO_2 adsorption properties of aerogels loaded with UiO-66, UiO-66-COOH, and UiO-66-2COOH (Fig. 1).

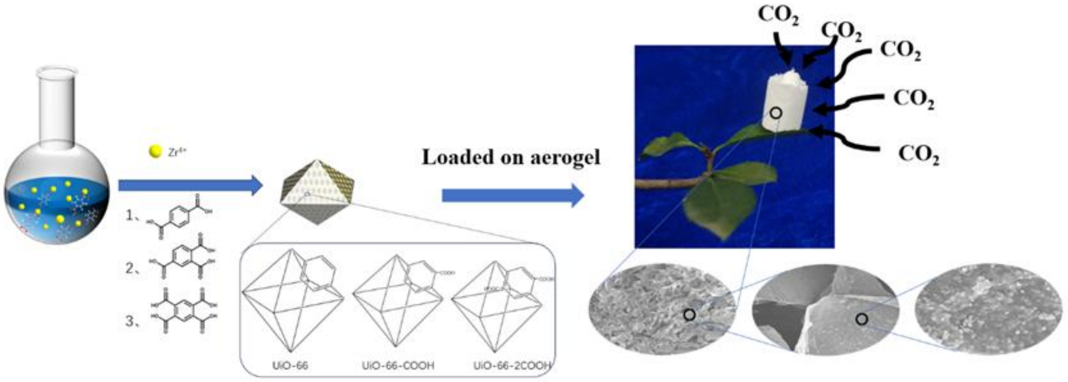

Fig. 2: Preparation process.

2. Materials and methods

2.1 MOF synthesis

UiO-66 Synthesis: 0.2332 g of $ZrCl_4$ and 0.1661 g of terephthalic acid were dissolved in 50 mL of N,N-Dimethylformamide (DMF) under ultrasonication for 10 minutes. The resultant solution was transferred to a 100 mL polytetrafluoroethylene-lined reactor and heated at 120 °C for 24 hours. After cooling, the product was purified by washing several times with DMF and methanol, followed by drying under vacuum at 120 °C for 24 hours (Fig. 2).

UiO-66-COOH Synthesis: 1.0500 g (5 mmol) of 1,2,4-benzenetricarboxylic acid and 1.2190 g (5 mmol) of $ZrCl_4$ were weighed into a 100 mL round-bottomed flask. Then, 30 mL of deionized water and 20 mL of acetic acid were added. The mixture was stirred at room temperature until fully dissolved, then heated to 100°C and refluxed for 24 hours. After cooling to room temperature, the solid was collected via high-speed centrifugation. It was washed several times with deionized water, soaked in methanol for 3 days with daily replacement, and finally dried at 120 °C for 24 hours (Fig. 2).

UiO-66-2COOH Synthesis: 1.2750 g (5 mmol) of 1,2,4,5-benzenetetracboxylic acid and 1.2190 g (5 mmol) of $ZrCl_4$ were weighed into a 100 mL round-bottomed flask. Then, 30 mL of deionized water and 20 mL of acetic acid were added. The mixture was stirred at room temperature until fully dissolved, then heated to 100 °C and refluxed for 24 hours. After cooling to room temperature, the solid was collected via high-speed centrifugation, washed several times with deionized water, soaked in methanol for 3 days with daily replacement, and finally dried at 120 °C for 24 hours (Fig. 2).

2.2 Preparation of composite aerogel（UiO-66-X/CA）

In the first step, $NHNH_2$-CMC was prepared as follows: 100g of Carboxymethyl cellulose (CMC) was dissolved in 100 mL of deionized water in a 150 mL round-bottomed flask and mixed using magnetic stirring at 200 rpm. Dihydrazide adipate was subsequently added to adjust the solution pH to approximately 7. N-hydroxysuccinimide (NHS) was dissolved in 4 mL of a 1:1 dimethyl sulfoxide (DMSO) /H_2O mixture and added dropwise to the CMC solution. Next, N'-(3-dimethylaminopropyl)-N-ethylcarbodiimide hydrochloride (EDC·HCl) was dissolved in 1 mL of a 1:1 DMSO/H_2O mixture and added to the CMC solution at room temperature. The pH of the resulting mixture was continuously adjusted to 6.8 using 0.1 M NaOH. The reaction proceeded for 1 hour under these conditions. The resultant polymer was dialyzed using a membrane tube with a molecular weight cutoff of 3500 Da in a spectroscopic laboratory. At least six dialysis cycles were performed before the solution was freeze-dried and stored.

The second step involved the preparation of aldehyde-based cellulose nanocrystals (CHO-CNCs). Cellulose nanocrystals (CNCs) were functionalized with aldehydes via sodium periodate oxidation at room temperature. Specifically, 0.5 g of CNCs (molecular weight 700 kDa) were dissolved in 50 mL of water. Sodium periodate (0.3 g) was then added and stirred at 200 rpm for 2 hours. Ethylene glycol (0.15 mL) was subsequently injected into the solution and reacted for 1 hour. The resulting polymer was dialyzed using a membrane tube with a molecular weight cutoff of 3500 Da, performing six dialysis cycles.

The third step focused on the preparation of the composite aerogel. MOF nanoparticles (0.1 g) were suspended in the previously prepared CHO-CNC suspension and sonicated for 15 minutes. The obtained suspension was mixed with an equal volume of the previously prepared $NHNH_2$-CMC solution and magnetically stirred for 2 minutes. It is important to note that MOFs must first be pre-mixed with a colloidal stabilized CHO-CNC suspension before being added to the CMC solution; otherwise, precipitation may occur if MOFs are directly added to the CMC solution. All suspensions were prepared in ultra-pure water without pH adjustment, and the natural pH of both CHO-CNC suspensions and $NHNH_2$-CMC solutions ranged between 5 and 6. The final cross-linked cluster suspension was transferred into a cylindrical glass vial (diameter 14.5 mm) and frozen for 12 hours at -20 °C. The ice gel was subsequently freeze-dried to obtain the final mixed aerogel. (Fig. 2)

The third step is the preparation of composite aerogels. Individually, 0.075 g, 0.1 g, and 0.125 g of MOF nanoparticles are suspended in the previously prepared CHO-CNC (0.05 g) suspension and sonicated for 15 minutes. The resulting suspensions are mixed with an equal volume of the previously prepared $NHNH_2$-CMC (0.05 g) solution and magnetically stirred for 2 minutes. It is critical that MOFs are first mixed with the stable CHO-CNC suspension before adding the CMC solution; direct addition of MOFs to the CMC solution may cause precipitation. All suspensions are prepared in ultrapure water without pH adjustment, with the natural pH values of the CHO-CNC suspension and $NHNH_2$-CMC solution ranging from 5 to 6. The final cross-linked cluster suspensions are transferred to cylindrical glass vials with a diameter of 14.5 mm and frozen at -20°C for 12 hours. Subsequently, the ice gels are freeze-dried to obtain the final hybrid aerogels UiO-66-X/CA (75%), UiO-66-X/CA (100%), and UiO-66-X/CA (125%) (Fig. 2).

2.3 Characterization

Field emission scanning electron microscopy (FE-SEM, Zeiss Sigma300) was employed to investigate the morphological characteristics of the samples. The Brunauer-Emmett-Teller (BET) specific surface area and pore size distribution were determined via nitrogen adsorption-desorption isotherm measurements at 77 K, using a Micromeritics 3Flex instrument. The crystalline structure and phase composition of MOFs and composite aerogel materials were analyzed by X-ray diffraction (XRD, Rigaku SmartLab), with a scanning angle (2θ) ranging from 5° to 50° and operating at 40 kV and 30 mA. The XRD patterns were recorded using the Rigaku SmartLab system. The thermal stability of the material under high-temperature conditions was evaluated using thermogravimetric analysis (TGA, TA Instruments SDT650, USA). Fourier-transform infrared spectroscopy (FT-IR, IR200) with a detection range of 400–4000 cm^{-1} was utilized to identify the functional groups in the MOFs and composite aerogel materials.

2.4 MOF stability test

UiO-66, UiO-66-COOH, UiO-66-2COOH were soaked in H_2SO_4 solution (pH=1), NaOH solution (pH=13), CH_3OH solution, and DMF solution for 5 hours, respectively. Then they were washed and dried, and the crystal structure and crystal state of the samples were determined by XRD.

2.5 GCMC simulate

Grand canonical Monte Carlo (GCMC) simulations were employed to investigate the adsorption process of carbon dioxide molecules onto the materials. All CO_2 adsorption simulations were conducted using the RASPA software in a code-based implementation, with the simulation temperature set to 273 K.[44] Each data point in the adsorption isotherms corresponds to the average loading value derived from 10,000 production cycles, with 10,000 initialization (equilibration) cycles performed prior to each production cycle (data not recorded). During simulations, adsorbate molecules were permitted to undergo translational motion, rotational motion, insertion, or removal from the rigid framework structure. Interactions between adsorbates and the framework were described using a Lennard-Jones (LJ) potential function with a cutoff radius of 12.0 Å, while long-range electrostatic interactions were treated via the Ewald summation method. Cross-interactions between distinct atoms followed the Lorentz-Berthelot combining rules.[45] The LJ parameters and charge values for CO_2 were sourced from the transferable phase equilibrium potential field (TraPPE),[46] whereas atomic parameters for MOF materials were adopted from classical universal force fields: UFF,[47] Dreiding,[48] and TraPPE-UA.[49] Atomic partial charges were determined using the DDEC6 method.[50] For simulation system construction, UiO-66, UiO-66-COOH, and UiO-66-2COOH were modeled using 2×2×2 supercell structures to perform adsorption calculations.

2.6 CO_2 adsorption

The CO_2 adsorption isotherms of MOFs and their composites were measured using a Micromeritics ASAP 2020 instrument (USA). Data were collected over a pressure range of 0 to 1 bar, and the isotherms were determined at 273 K and 298 K. Approximately 0.5 g of each sample was activated under vacuum conditions at 120 °C for 12 hours prior to measurement. The heat of adsorption for the MOFs was calculated by fitting the CO_2 adsorption isotherms at 273 K and 298 K. Ultra-high purity CO_2 (purity ≥ 99.999%) was used for the adsorption measurements.

2.7 CO_2/N_2 adsorption selectivity simulation

Adsorption isotherms of N_2 and O_2 on MOF and composites were determined using a Micromeritics ASAP 2020 (USA) instrument. Data were collected over the pressure range of 0 to 1 bar, and the adsorption isotherms of the samples were determined at 273 K. Each sample (approximately 0.5 g) was activated under vacuum at 120 °C for 12 hours and tested using high-purity N_2 and O_2 as adsorbates. Using the adsorption curves of the samples at 273 K for pure CO_2 and N_2, the adsorption amounts of CO_2 and N_2 in a mixture ($CO_2/N_2 = 15/85$, v/v) were predicted using the Ideal Adsorbed Solution Theory (IAST) based on pure-component adsorption data.

2.8 CO_2/N_2 Breakthrough Experiments of UiO-66-2COOH/AC

The breakthrough experiment was conducted in a dynamic gas breakthrough device. The sample was packed into stainless steel columns with a length of 126 mm and an inner diameter of 10 mm. The activated UiO-66-2COOH/AC sample (1.12 g) was loaded into the column, and the two ends of the column were sealed with absorbent cotton. The column was placed in a circulating jacket and connected to a constant-temperature bath to control the temperature at 273 K under a pressure of 1 bar. The flow rate and pressure of the mixed gas were controlled via a pressure control valve and a mass flow controller. The gas composition was $CO_2:N_2 = 15:85$ (v/v), with a total flow rate of 3.33 sccm ($CO_2 = 0.2$ sccm, $N_2 = 2.83$

sccm). Two test conditions were selected: dry conditions and a relative humidity (RH) of 50%. Continuous monitoring was performed using a gas analysis mass spectrometer. CO_2 breakthrough was determined when the outlet gas composition matched the inlet gas composition. The "CO_2/N_2 breakthrough time" is defined as the time interval between the breakthrough of N_2 and CO_2.

3. Results and discussion

3.1 UiO-66-X characterization results

The XRD patterns of UiO-66, UiO-66-COOH, and UiO-66-2COOH are shown in Fig. 3(a). The synthesized UiO-66 showed typical peaks at $2\theta=7.4°$, 8.5°, 14.9°, 17.1°, 25.9°, and 31.1°, corresponding to the (111), (200), (222), (400), (442), and (711) crystal planes. These results confirm the successful synthesis of UiO-66. The XRD patterns of UiO-66-COOH and UiO-66-2COOH precisely matched those of UiO-66, indicating that the introduction of carboxyl groups did not alter the crystal structure. In the FTIR spectra of UiO-66-COOH and UiO-66-2COOH, the characteristic peak at 1710 cm^{-1} was attributed to the C=O stretching vibration of the free carboxyl group, verifying the successful carboxylation of UiO-66. The peak around 1590 cm^{-1} corresponds to the stretching vibration of O-C-O. The peaks around 1513 cm^{-1} and 1440 cm^{-1} are assigned to the vibration of the benzene ring skeleton, while the peaks around 1040 cm^{-1} and 1020 cm^{-1} correspond to C-O bending and stretching vibrations. The peaks around 803 cm^{-1}, 663 cm^{-1}, and 771 cm^{-1} are attributed to Zr-O/Zr-O_2 stretching vibrations (Fig. 3(b)).

The thermogravimetric analysis-derivative thermogravimetry (TGA-DTG) curves of UiO-66, UiO-66-COOH, and UiO-66-2COOH samples are shown in Fig. 3(c). The guest molecule (H_2O) was lost between 25 °C and 100 °C (12%), and the free acid remaining in the pores was lost between 100 °C and 400 °C (15%). The third weight loss occurred between 400 °C and 500 °C, corresponding to the degradation of the skeleton to produce ZrO_2. The crystal morphology of UiO-66, UiO-66-COOH, and UiO-66-2COOH is shown in Fig. 4. UiO-66 exhibits uniform crystallinity, a smooth surface, and a square shape, with a particle size of about 150–300 nm. The UiO-66-COOH and UiO-66-2COOH samples show uniform crystallinity, smooth surfaces, and spherical shapes. The particle size of UiO-66-COOH is approximately 150–300 nm, while the particle size of UiO-66-2COOH is approximately 150–300 nm. The elemental contents of UiO-66, UiO-66-COOH, and UiO-66-2COOH samples are shown in Table 1. It can be found that the three materials are mainly composed of Zr, C, and O elements, with similar elemental contents across the three materials. EDS elemental distributions in the UiO-66, UiO-66-COOH, and UiO-66-2COOH samples are shown in Fig. 4 (d- f). Zr, C, and O are evenly distributed throughout the samples without obvious segregation.

The N_2 adsorption-desorption isotherms of samples are shown in Fig. 5(a). The nitrogen isotherms of UiO-66, UiO-66-COOH, and UiO-66-2COOH indicate a typical Type I isotherm (according to the IUPAC) without a clear hysteresis loop, signifying the presence of micropore structure in all three materials. The BET surface areas of UiO-66, UiO-66-COOH, and UiO-66-2COOH are 890.91 m^2/g, 374.74 m^2/g, and 696.75 m^2/g, respectively. Notably, the introduction of carboxyl groups in UiO-66-COOH leads to a significant decrease in surface area, possibly due to partial pore blockage or structural shrinkage, while UiO-66-2COOH maintains a higher surface area, suggesting a balance between functionalization and pore retention.

The specific surface area and the ratio of micropore surface area to total BET surface area (S_{micro}/S_{BET}) of the samples are

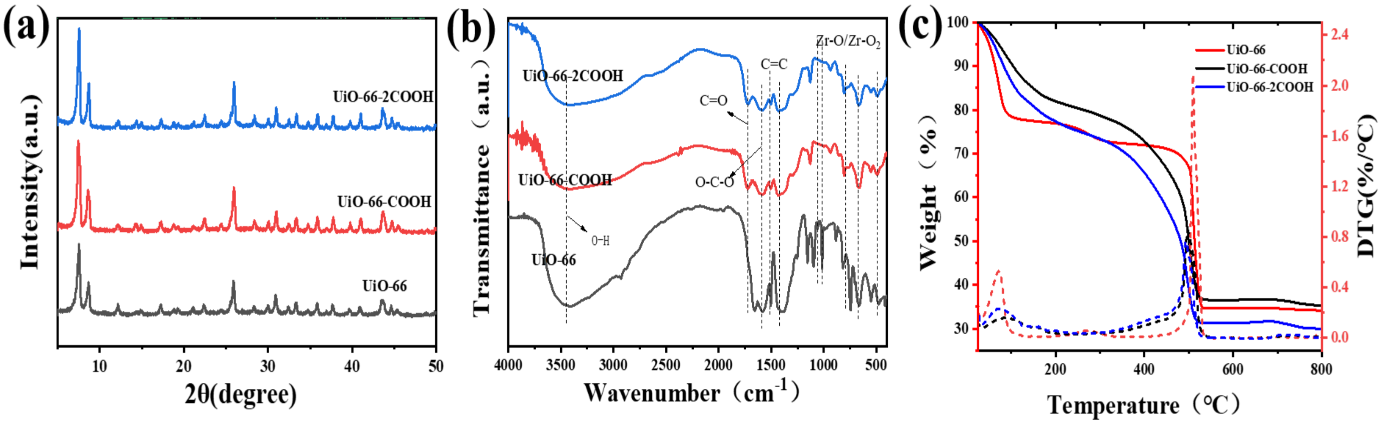

Fig. 3: (a) XRD patterns, (b) FT-IR spectra, and (c) TGA-DTG curves of UiO-66, UiO-66-COOH, UiO-66-2COOH samples.

Table 1: UiO-66、UiO-66-COOH、UiO-66-2COOH sample element content.

Sample	C（Wt%）	O（Wt%）	Zr（Wt%）
UiO-66	61.8	22.7	15.6
UiO-66-COOH	72.4	16.5	10.7
UiO-66-2COOH	75.4	15.5	9.1

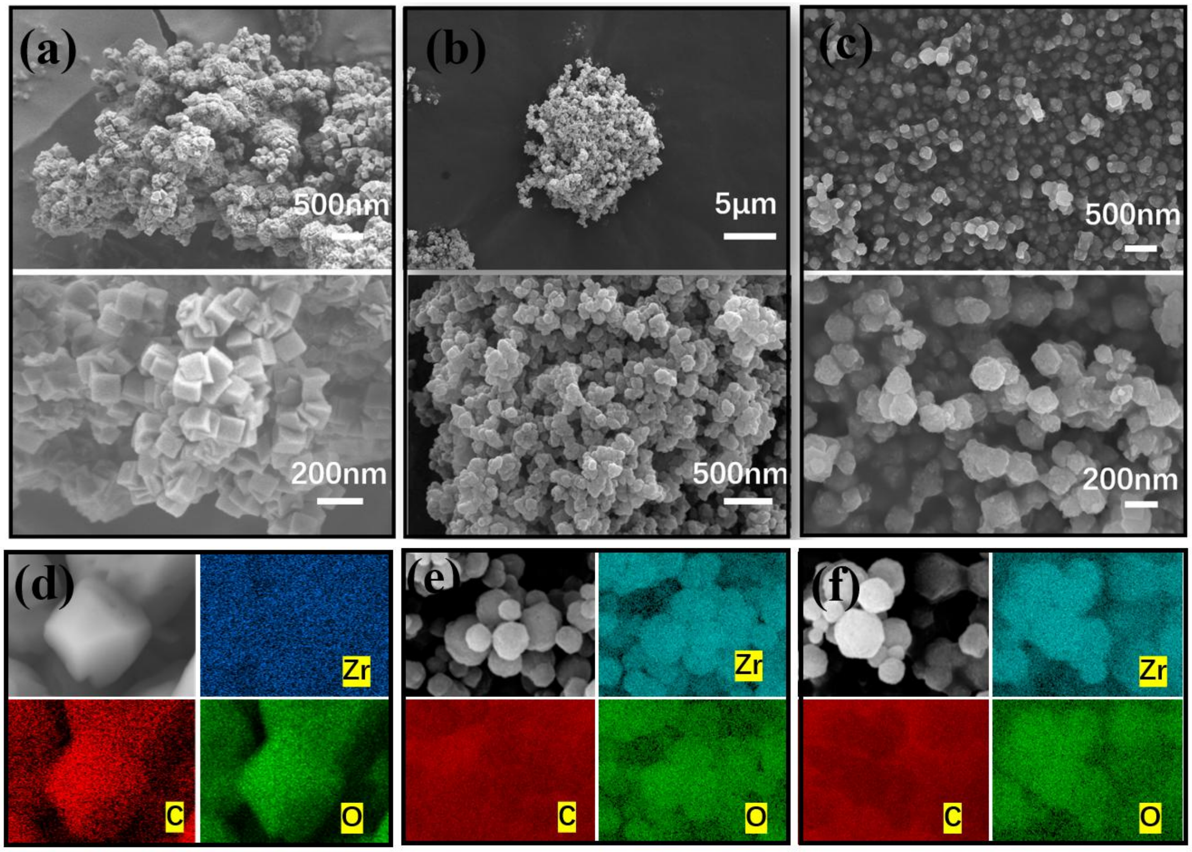

Fig. 4: SEM image of (a) UiO-66, (b) UiO-66-COOH and (c) UiO-66-2COOH, EDS distribution map of (d) UiO-66, (e) UiO-66-COOH and (f) UiO-66-2COOH.

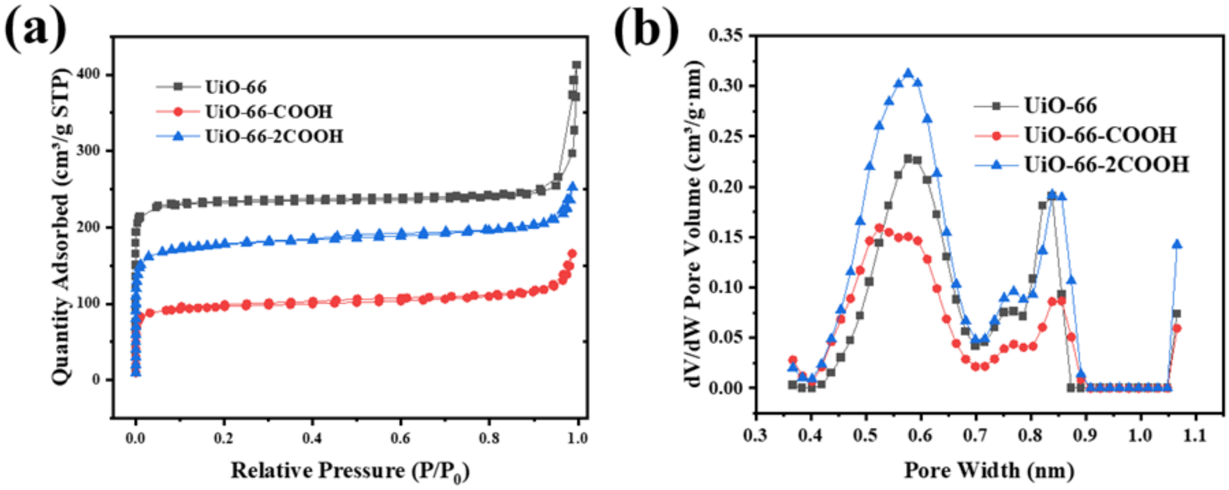

Fig. 5: (a) Nitrogen adsorption isotherms of UiO-66, UiO-66-COOH, and UiO-66-2COOH at T = 77 K (P0 = 1 atm); (b) The micropore pore size distributions of UiO-66, UiO-66-COOH, and UiO-66-2COOH were obtained by calculating the experimental data of the CO_2 (273 K) adsorption isotherm using the DFT model.

Table 2: UiO-66、UiO-66-COOH、UiO-66-2COOH architectural feature.

Sample	Specific surface area (m^2/g)	Specific surface area of micropores (m^2/g)	S_{micro}/S_{BET} (%)
UiO-66	890.91	871.76 m^2/g	97.85%
UiO-66-COOH	374.74	290.70m^2/g	77.57%
UiO-66-2COOH	696.75	538.81 m^2/g	77.33%

presented in Table 2. As shown, the micropore surface area of UiO-66-COOH and UiO-66-2COOH accounts for approximately 77% of the total surface area, whereas that of UiO-66 constitutes 97.85%. The pore size distributions of UiO-66, UiO-66-COOH, and UiO-66-2COOH were obtained by applying the HK model to the N_2 (77 K) adsorption isotherm (Fig. S1). The pores of UiO-66 are mainly distributed at approximately 0.67 nm and 0.85 nm, those of UiO-66-COOH at ~0.7 nm, and those of UiO-66-2COOH at ~0.75 nm and 1.1 nm. Carbon dioxide adsorption was chosen for pore size analysis because CO_2 molecules have a small kinetic diameter (~0.33 nm) and can effectively diffuse into ultramicropores at 273 K. In contrast, nitrogen cannot enter the pores at 77 K due to low-temperature kinetic limitations. Analysis of carbon dioxide adsorption accurately measures pore size distributions from 0.4 to 1 nm. In Fig. 5(b), the ultramicropore size distributions of UiO-66, UiO-66-COOH, and UiO-66-2COOH were obtained by modeling the experimental data of the CO_2 adsorption isotherm at 273 K using the DFT model. All three samples exhibit peak values around 0.55 nm and 0.85 nm.

The XRD patterns of UiO-66, UiO-66-COOH, and UiO-66-2COOH obtained after soaking in H_2SO_4 solution (pH=1), NaOH solution (pH=13), CH_3OH solution, and DMF solution for 5 hours, respectively (Figs. S2, S3, S4) can be found. The XRD patterns of UiO-66, UiO-66-COOH, and UiO-66-2COOH in H_2SO_4 solution (pH=1), CH_3OH solution, and DMF solution showed no significant changes, while the XRD patterns of UiO-66 in NaOH solution (pH=13) were weakened, but the position of the peaks did not change. This indicates that its structure can exist stably. In contrast, the XRD patterns of UiO-66-COOH and UiO-66-2COOH exhibited weakened intensities, sharpened peaks, and disappeared small peaks, suggesting that their structures were partially altered. The reason is that NaOH reacts with the carboxyl groups introduced on the pore walls of the MOF, thus destroying the MOF structure. This study systematically evaluated the stability of UiO-66, UiO-66-COOH, and UiO-66-2COOH in various solvents and under acidic/alkaline conditions. The results revealed that these materials demonstrated good chemical stability, implying their potential applicability in diverse media.

3.2 GCMC simulation results

To further clarify the performance relationship between carbon dioxide adsorption and framework materials, Grand Canonical Monte Carlo (GCMC) simulation methods were employed for research under low-pressure conditions of 273 K and $P/P_0 = 0.1$. The results show that the simulated adsorption capacities of UiO-66, UiO-66-COOH, and UiO-66-2COOH (Fig. 6(a-b) shows the distribution diagram of CO_2 in the 2×2×2 supercell structures of UiO-66, UiO-66-COOH, and UiO-66-2COOH) are 7.20 cm^3/g, 11.28 cm^3/g, and 19.34 cm^3/g, respectively, which are basically consistent with the experimental values of 8.9 cm^3/g, 11.24 cm^3/g, and 19.7 cm^3/g. The analysis of adsorption sites indicates that there are three types of interaction forces between UiO-66 and carbon dioxide ($O_{CO_2}\cdots\pi_{BDC}$, $O_{CO_2}\cdots C_{BDC}$, $O_{CO_2}\cdots H_{BDC}$) (Fig. 6(d)). Among them, the interaction distance of $O_{CO_2}\cdots\pi_{BDC}$ is 3.81–3.95 Å (Fig. S5(b)), the interaction distance of $O_{CO_2}\cdots C_{BDC}$ is 3.58–3.91 Å (Fig. S5(c)), and the interaction distance of $O_{CO_2}\cdots H_{BDC}$ is 3.81–3.84 Å (Fig. S5(d)). The distance between the framework and the guest molecules is relatively far, and there are weaker interaction forces, resulting in low adsorption capacity.

We performed GCMC simulations on the structurally modified UiO-66-COOH and identified five types of interaction forces ($O_{CO_2}\cdots\pi_{BDC}$, $O_{CO_2}\cdots C_{BDC}$, $O_{CO_2}\cdots H_{BDC}$, $O_{CO_2}\cdots O_{BDC}$, $O_{CO_2}\cdots C_{CO_2}$) (Fig. 6(c)). Among them, the interaction distance of $O_{CO_2}\cdots\pi_{BDC}$ is 3.71 Å (Fig. S6(b)), the interaction distance of $O_{CO_2}\cdots C_{BDC}$ is 3.01–3.79 Å (Fig. S6(c)), the interaction distance of $O_{CO_2}\cdots H_{BDC}$ is 3.02–3.80 Å (Fig. S6(d)), the interaction distance of $O_{CO_2}\cdots O_{BDC}$ is 3.35–3.76 Å (Fig. S6(e)), and the interaction distance of $O_{CO_2}\cdots C_{CO_2}$ is 3.11–3.24 Å (Fig. S6(f)). Compared with UiO-66, UiO-66-COOH exhibits more types of adsorption interactions with carbon dioxide and a higher density of interaction forces, indicating that the modification of carboxyl groups enhances the interaction with carbon dioxide and can adsorb more carbon dioxide molecules, which is consistent with the experimental adsorption structure.

Subsequently, we conducted site simulations on UiO-66$(COOH)_2$ modified with two carboxylic acid groups and identified five types of interaction forces: $O_{CO_2}\cdots\pi_{BDC}$, $O_{CO_2}\cdots C_{BDC}$, $O_{CO_2}\cdots H_{BDC}$, $O_{CO_2}\cdots O_{BDC}$, and $O_{CO_2}\cdots C_{CO_2}$ (Fig. 6(e)). Among them, the interaction distance of $O_{CO_2}\cdots\pi_{BDC}$ is 3.34–3.96 Å (Fig. S7(b)), that of $O_{CO_2}\cdots C_{BDC}$ is 3.09–3.70 Å (Fig. S7(c)), $O_{CO_2}\cdots H_{BDC}$ is 2.95–3.97 Å (Fig. S7(d)), $O_{CO_2}\cdots O_{BDC}$ is 3.28–3.90 Å (Fig. S7(e)), and $O_{CO_2}\cdots C_{CO_2}$ is 3.02–3.90 Å (Fig. S7(f)). Notably, the count of $O_{CO_2}\cdots O_{BDC}$ interactions reaches 14, which is higher than that in the parent material UiO-66 and UiO-66-COOH. This phenomenon is primarily attributed to the modification of two carboxylic acid groups on the BDC ligand, which enhances the interaction between guest CO_2 molecules and the framework, thereby leading to a higher final adsorption capacity than the other two materials.

Additionally, we visualized the adsorption behavior of the three materials within a single unit cell and found that the adsorption capacity increases sequentially from the parent UiO-66 to carboxyl-modified UiO-66-COOH and then to di-carboxyl-modified UiO-66-2COOH. Due to the strong guest–framework interactions, the tetrahedral cages of UiO-66-COOH exhibit aggregation of guest molecules, while UiO-66-2COOH shows guest molecule aggregation across multiple tetrahedral cages. This observation is consistent with the finding that UiO-66-2COOH demonstrates the highest adsorption capacity under the same pressure.

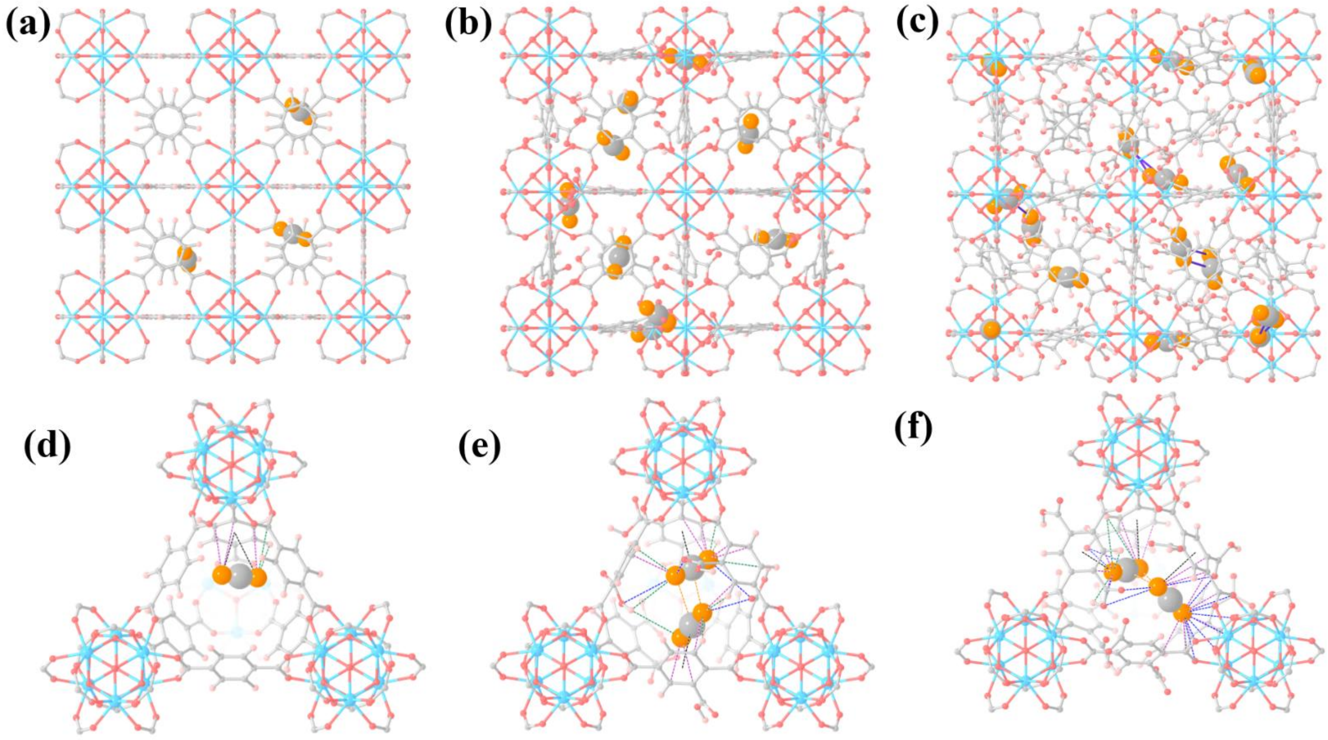

Fig. 6: (a) UiO-66 2×2×2 supercell structures Adsorb carbon dioxide; (b) UiO-66-COOH 2×2×2 supercell structures Adsorb carbon dioxide; (c) UiO-66-2COOH 2×2×2 supercell structures Adsorb carbon dioxide; (d) All the interactions between UiO-66 and CO_2; (e) All the interactions between UiO-66-COOH and CO_2;(f) All the interactions between UiO-66-2COOH and CO_2.(Black is $O_{CO_2}\cdots\pi_{BDC}$, purple is $O_{CO_2}\cdots C_{BDC}$, green is $O_{CO_2}\cdots H_{BDC}$, blue is $O_{CO_2}\cdots O_{BDC}$, and orange is $O_{CO_2}\cdots O_{CO_2}$)

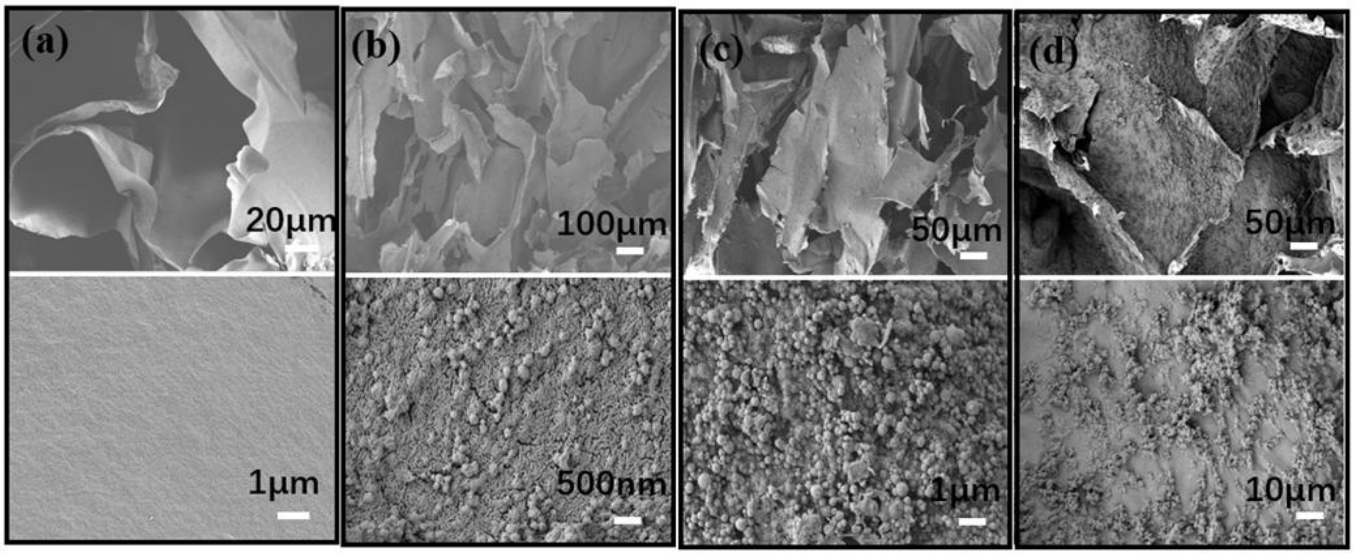

Fig. 7: SEM of (a) CA; (b) UiO-66/CA; (c) UiO-66-COOH/CA; (d) UiO-66-2COOH/CA.

3.3 UiO-66-X/CA characterization results

The XRD pattern of UiO-66-X/CA shows clear peaks at 7.4, 8.5, and 25.9 (Fig. S8), indicating successful MOF loading and that the MOF structure remained intact during the loading process. By providing a rigid structure, the addition of MOF facilitates the molding of aerogels, while unladen CA aerogels are difficult to mold (Fig. S9). The FTIR spectrum of modified CNC (Fig. S10) shows characteristic peaks for aldehyde groups at 1640 cm^{-1} and C-H stretching vibrations of aldehyde groups at 2850 cm^{-1}, indicating successful introduction of aldehyde groups. The FTIR spectrum of modified CMC (Fig. S11) shows carbonyl bond peaks (amide bonds formed between ADH and CMC) at 1630 cm^{-1}, acetate group-specific peaks at 1242 cm^{-1}, and N-H bond stretching vibration peaks at 3200–3300 cm^{-1}, indicating successful introduction of hydrazide groups. The FTIR spectrum of CNC-C=NNH-CMC

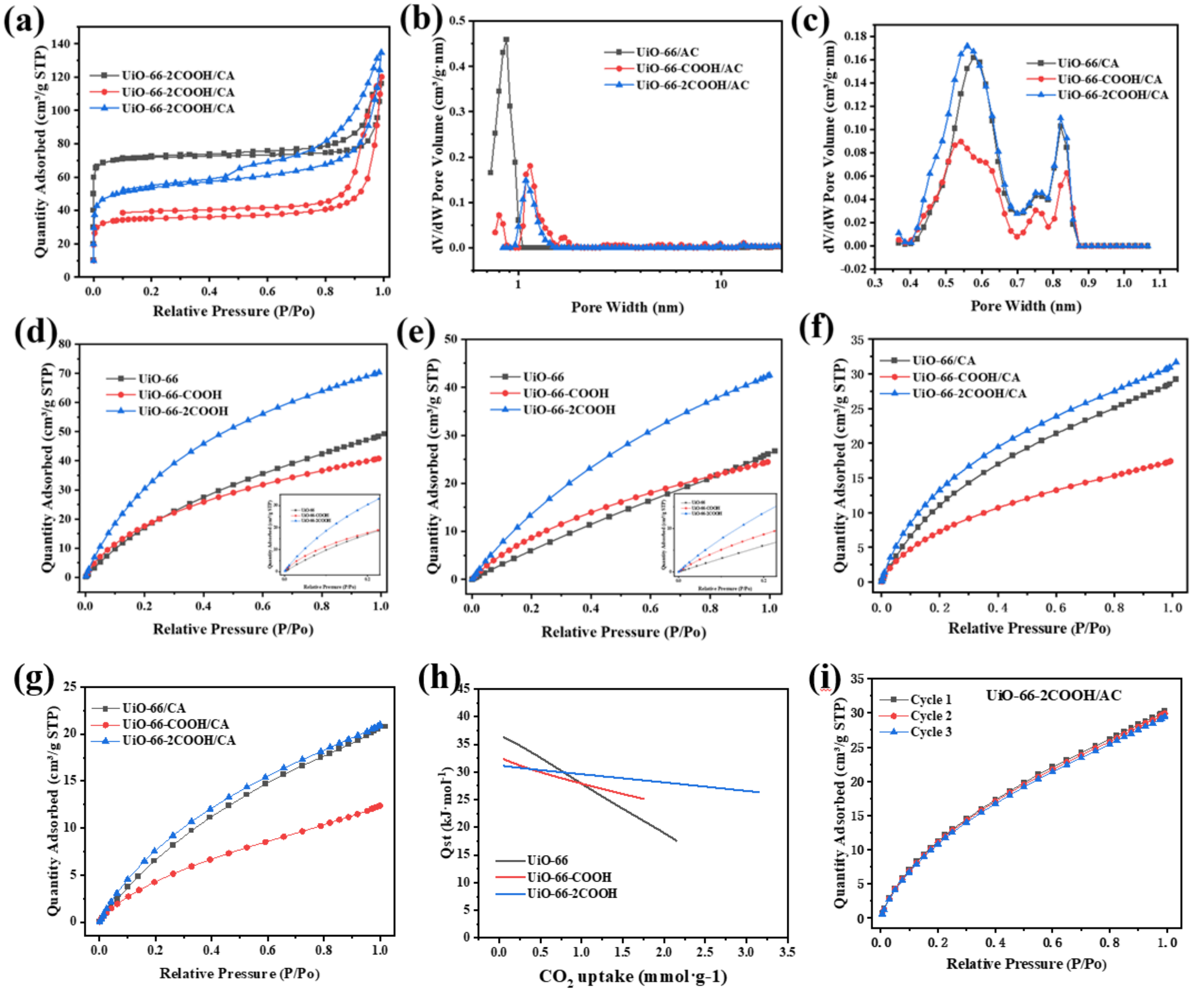

Fig. 8: (a) Nitrogen adsorption isotherms of UiO-66/CA、UiO-66-COOH/CA、UiO-66-2COOH/CA at T=77K (P0 = 1atm); (b) The DTF model was used to calculate the experimental data of N_2 (77 K) adsorption isotherm, and the micropore pore size distribution of the loaded UiO-66, UiO-66-COOH and UiO-66-2COOH aerogel was obtained; (c) The DFT model was used to calculate the experimental data of CO_2 (273 K) adsorption isotherm, and the ultramicropore pore size distribution of UiO-66/CA、UiO-66-COOH/CA, and UiO-66-2COOH/CA were obtained. (d, e) CO_2 adsorption isotherms of UiO-66, UiO-66-COOH, UiO-66-2COOH at 273K and 298K; (f, g) CO_2 adsorption isotherms of UiO-66 /CA, UiO-66-COOH /CA, UiO-66-2COOH /CA at 273K and 298K; (h) Equivalent heat of CO_2 adsorption (Qst); (i) carbon dioxide repeated adsorption test (273K).

(Fig. S12) shows C=N stretching vibration peaks at 1635 cm^{-1}, indicating successful cross-linking.

Fig. 7(a-d) shows the morphologies of CA, UiO-66/CA, UiO-66-COOH/CA, and UiO-66-2COOH/CA. The cellulose aerogel exhibits a sheet-like structure. Compared to the MOF-loaded aerogels, the unloaded cellulose aerogel features a smooth surface, whereas the loaded counterparts exhibit a rough texture, which increases the adsorption sites for target substances. The three MOF materials are evenly distributed on the aerogel with good dispersion and no obvious agglomeration.

Compared to the 100% loading samples, the morphologies of UiO-66/CA (75%), UiO-66-COOH/CA (75%), and UiO-66-2COOH/CA (75%) showed sparser MOF particle distribution on the aerogel (Fig. S13). In contrast, UiO-66/CA (125%), UiO-66-COOH/CA (125%), and UiO-66-2COOH/CA (125%) exhibited an increase in MOF particle loading compared to the 100% loading samples, accompanied by phenomena such as agglomeration (Fig. S14).

The nitrogen isotherms of UiO-66/CA, UiO-66-COOH/CA, and UiO-66-2COOH/CA indicated a typical Type I isotherm (according to the IUPAC) with a clearly visible hysteresis loop, indicating the existence of mesoporous structures. Fig. 8(a) The specific surface areas were 286.04 m²/g, 201.36 m²/g, and 137.29 m²/g, respectively. When $P/P_0 < 0.1$, the rapid increase in nitrogen adsorption amount indicated the presence of abundant micropores, which provide numerous adsorption sites. This is crucial for enhancing the adsorption thermodynamics of the materials. The adsorption and desorption curves formed an obvious hysteresis loop, indicating the presence of mesopores. This feature accelerates the mass transfer of the adsorbent to the adsorption sites and enhances the adsorption kinetics of the material. From Fig. 8(b), it can be found that UiO-66/CA, UiO-66-COOH/CA, and UiO-66-2COOH/CA materials have a large number of pores in the range of 0.8–2 nm. The DFT model was used to calculate the experimental data of the CO_2 (273 K) adsorption isotherm, and obtained the ultrapore pore-size distributions of UiO-66/CA, UiO-66-COOH/CA, and UiO-66-2COOH/CA (Fig. 8(c)). Comparison with Fig. 5(b) shows that the pore size distribution remained basically unchanged. It further indicates that the MOF is successfully loaded on the aerogel, with the micropores provided by the loaded MOF, and the spatial structure of the MOF is not destroyed during the loading process.

3.4 CO_2 adsorption

Fig. 8(d) shows the CO_2 adsorption isotherms of UiO-66, UiO-66-COOH, and UiO-66-2COOH at 273 K. The adsorption capacities were 41.26 cm³/g, 25.3 cm³/g, and 70.4 cm³/g, respectively. Compared with UiO-66, the CO_2 adsorption capacity of UiO-66-COOH decreased by 39%, while that of UiO-66-2COOH increased by 71%. Fig. 8(e) shows the isotherms at 298 K, with capacities of 29.2 cm³/g, 25.7 cm³/g, and 42.5 cm³/g. UiO-66-COOH exhibited a 12% decrease, while UiO-66-2COOH showed a 46% increase.

Compared with UiO-66, UiO-66-COOH and UiO-66-2COOH feature abundant carboxyl groups on their pore walls, with UiO-66-2COOH containing exactly twice the carboxyl groups of UiO-66-COOH. These groups interact with CO_2 through specific forces, enhancing adsorption. The BET surface areas were 890.91 m²/g, 374.74 m²/g, and 696.75 m²/g. Although UiO-66-2COOH's surface area decreased by 21.8% (likely due to carboxyl-induced pore contraction), its higher carboxyl abundance outweighed the surface area loss, leading to enhanced adsorption. In contrast, UiO-66-COOH suffered a 57.9% surface area reduction and lower carboxyl density, resulting in diminished capacity.

The initial Qst values of UiO-66, UiO-66-COOH, and UiO-66-2COOH were 36.3, 32.3, and 31.1 $kJ\cdot mol^{-1}$, respectively (Fig. 8(h)), indicating that CO_2 was physically adsorbed on the material ($\Delta H < 40\ kJ\cdot mol^{-1}$). It can be obviously observed that with the increase of pressure, the adsorption heat of UiO-66 decreased the fastest, followed by UiO-66-COOH, while that of UiO-66-2COOH decreased more slowly. The interaction strength between surface functional groups (e.g., carboxyl groups) and adsorbed substances also influenced the rate of change in adsorption heat. This is because stronger interactions between functional groups and adsorbates may lead to a slower decrease in adsorption heat.

Fig. 8(g) shows the CO_2 adsorption isotherms of UiO-66/CA, UiO-66-COOH/CA and UiO-66-2COOH/CA at 298 K, with adsorption capacities of 20.8 cm³/g, 12.4 cm³/g and 21.0 cm³/g, respectively. The CO_2 adsorption capacity of UiO-66-COOH/CA decreased by 40% compared with UiO-66/CA, and the CO_2 adsorption capacity of UiO-66-2COOH/CA increased by 1% compared with UiO-66/CA. Compared to pure MOFs, the CO_2 adsorption capacity of MOF-loaded aerogels is reduced because the aerogel matrix dilutes the MOF content. As the primary adsorbent, MOF dominates CO_2 uptake, while the aerogel serves only as a support with negligible adsorption, thus diluting the total adsorption capacity. At 273 K, the CO_2 adsorption capacities of UiO-66/CA (75%), UiO-66-COOH/CA (75%), and UiO-66-2COOH/CA (75%) are 16.4 cm³/g, 11.0 cm³/g (Fig. S15), and 21.0 cm³/g, respectively. At 273 K, the CO_2 adsorption capacities of UiO-66/CA (125%), UiO-66-COOH/CA (125%), and UiO-66-2COOH/CA (125%) are 18.6 cm³/g, 12.8 cm³/g, and 24.6 cm³/g (Fig. S16), respectively. Notably, the CO_2 adsorption capacity of aerogels with 75% and 125% loadings is lower than that with a 100% loading. Fig. 8(i) shows the three adsorption cycles of CO_2 in Uio-66-2COOH/CA. This sample maintains its adsorption performance and exhibits excellent stability, recoverability and durability.

3.5 CO_2/N_2 adsorption selectivity simulation

Fig. 9(a-c) shows the adsorption isotherms of CO_2, N_2, and O_2 for three MOF materials at 273 K. For UiO-66, the CO_2 adsorption capacity is 12.3 and 18.3 times that of N_2 and O_2, respectively. UiO-66-COOH exhibits CO_2 adsorption capacities 13.6 times that of N_2 and 18.5 times that of O_2. UiO-66-2COOH shows even higher selectivity, with CO_2 adsorption capacities 18.1 and 27.1 times those of N_2 and O_2, respectively. Fig. 10(a-c) illustrates the adsorption isotherms of CO_2, N_2, and O_2 for the three MOF/AC composite materials at 273 K. UiO-66/AC demonstrates CO_2 adsorption capacities 12.7 and 14.6 times those of N_2 and O_2, respectively. In contrast, UiO-66-COOH/AC shows lower selectivity, with CO_2 adsorption capacities 7.9 and 8.6 times that of N_2 and O_2. UiO-66-2COOH/AC balances performance, achieving CO_2 adsorption capacities 13.7 and 16.6 times those of N_2 and O_2, respectively.

To evaluate the adsorption selectivity of MOFs, the pure-component IAST was applied. The data were derived from the CO_2 and N_2 adsorption isotherms at 273 K, and subsequently fitted to the two-site Langmuir-Freundlich (DSLF) model. IAST describes the equilibrium between the ideal adsorption solution and the ideal gas phase, enabling the prediction of adsorption behavior for mixtures based solely on pure-component adsorption isotherms.

According to the composition of the flue gas, 15% CO_2 and 85% N_2 were selected to predict the gas separation performance. As shown in Fig. 9(d-f), when the pressure

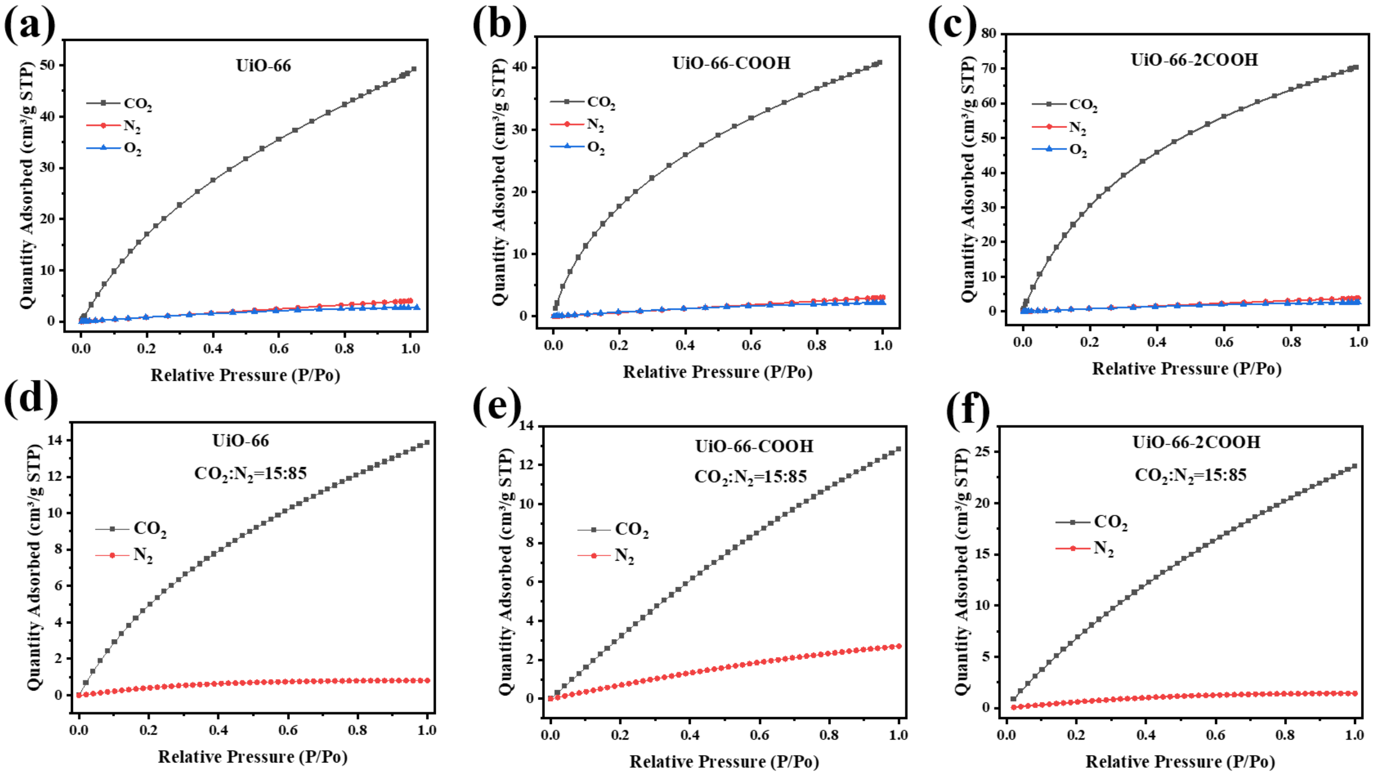

Fig. 9: (a, b, c) Adsorption isotherms of CO_2, N_2 and O_2 of UiO-66, UiO-66-COOH and UiO-66-2COOH at 273K; (d, e, f) Prediction results of adsorption of CO_2 and N_2 by UiO-66, UiO-66-COOH and UiO-66-2COOH at 273K and CO_2: N_2=15:85.

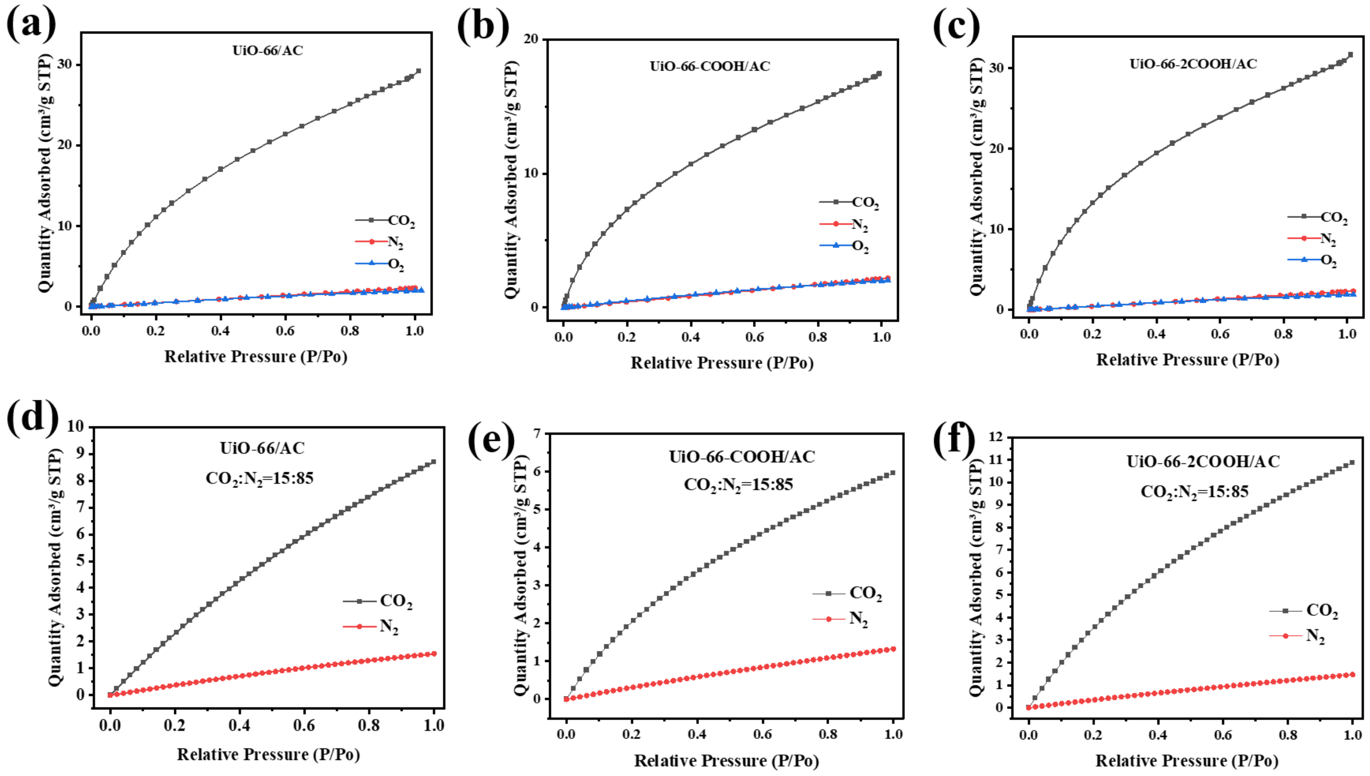

Fig.10: (a, b, c) adsorption isotherms of CO_2, N_2, and O_2 of UiO-66/AC, UiO-66-COOH/AC, and UiO-66-2COOH/AC at 273K; (d, e, f) Prediction results of adsorption of CO_2 and N_2 by UiO-66/AC, UiO-66-COOH/AC, UiO-66-2COOH/AC at 273K and CO_2: N_2=15:85; (g, h) selectivity of UiO-66-X and UiO-66-X/AC (CO_2:N_2=15:85), (i) Breakthrough curves for CO2 and N2 (15/85, v/v) at 293 K and 1 bar.

reached normal pressure, the carbon dioxide adsorption capacities of UiO-66, UiO-66-COOH and UiO-66-2COOH were 12.8 cm^3/g, 13.9 cm^3/g and 23.6 cm^3/g, respectively. These values were 4.7 times the nitrogen adsorption capacity (2.7 cm^3/g), 17.4 times (0.8 cm^3/g), and 16.6 times (1.4 cm^3/g). The selectivity of carboxyl-modified MOF decreased first and then increased with increasing pressure, and the selectivities at atmospheric pressure were 26.8, 97.1 and 93.2, respectively (Fig. 10(g)). It can be seen that the selectivity of carboxyl-modified MOF under atmospheric pressure exceeded 90, demonstrating relatively high selective adsorption performance for carbon dioxide, which is attributed to the higher affinity of carboxyl groups for CO_2. As depicted in Fig. 10(d-f), when the pressure reached atmospheric pressure, the CO_2 adsorption capacities of UiO-66/AC, UiO-66-COOH/AC, and UiO-66-2COOH/AC were 8.7 cm^3/g, 6.0 cm^3/g, and 10.9 cm^3/g, respectively, corresponding to 5.8 times (1.5 cm^3/g), 4.6 times (1.3 cm^3/g), and 7.3 times (1.5 cm^3/g) the nitrogen adsorption capacity. The selectivities at atmospheric pressure were 25.6, 31.8, and 41.9 for UiO-66/AC, UiO-66-COOH/AC, and UiO-66-2COOH/AC, respectively (Fig. 10(h)). The incorporation of cellulose aerogel reduced the material's selectivity, indicating that the MOF was primarily loaded onto the cellulose aerogel, which served only as a carrier and exhibited no selective affinity for CO_2. This study provides valuable insights into the selective capture of carbon dioxide from flue gas.

3.6 CO_2/N_2 Breakthrough Experiments of UiO-66-2COOH/AC

Competitive water adsorption is a challenge in developing new adsorbents for carbon capture, so it is necessary to analyze these adsorbents' performance under wet conditions. In all the breakthrough experiments (Fig. 10(i)), N_2 was first eluted from the packed column until adsorption equilibrium was reached, while CO_2 took a longer time to penetrate the column, demonstrating the framework's ability to separate the two gases. Notably, N_2 exhibits a "delayed breakthrough" behavior, typical of carbon dioxide displacing small amounts of adsorbed N_2 in a binary gas mixture. Under dry conditions, the penetration times of N_2 and CO_2 were 3.6 and 637 s, respectively; the CO_2 adsorption capacity was 8.93 cm^3/g, and the CO_2/N_2 separation coefficient was 55.49. Under 50% relative humidity (humid conditions), the penetration times of N_2 and CO_2 were 3.4 and 613 s, respectively. Compared with dry conditions, the CO_2 penetration time shortened by 24 s (3.7%), the CO_2 adsorption capacity decreased to 8.04 cm^3/g, indicating that water competed for adsorption sites with CO_2. The CO_2/N_2 separation coefficient under humid conditions was 49.53. Although humidity had a moderate impact, UiO-66-2COOH/AC still distinguished between carbon dioxide and nitrogen, shortening the CO_2 penetration time by 3.7%. Overall, these findings indicate that UiO-66-2COOH/AC exhibits selective adsorption properties and favors carbon dioxide under both dry and humid conditions.

4. Conclusion

In this study, we successfully prepared UiO-66, UiO-66-COOH, and UiO-66-2COOH with excellent thermal stability, extremely high chemical stability, high specific surface area and porosity, and good mechanical stability. The BET specific surface area of UiO-66-2COOH (696.75 m^2/g) was smaller than that of UiO-66 (890.91 m^2/g), but the CO_2 adsorption of synthesized UiO-66-2COOH reached 70.4 cm^3/g at 273 K, while UiO-66 was only 41.3 cm^3/g. The presence of carboxyl groups increases the polarity of the adsorbent surface, thereby enhancing the van der Waals interaction between the surface and CO_2 molecules and improving the CO_2 adsorption capacity. Under low-pressure conditions (273 K, $P/P_0 = 0.1$), the CO_2 adsorption performance of the UiO-66 series was studied via GCMC simulation. The results show that the simulated adsorption amounts agree with the experimental values. With an increase in the number of carboxyl modifications (from UiO-66 to UiO-66-COOH and then to UiO-66-2COOH), the simulated adsorption amount increased from 7.20 to 19.34 cm^3/g. Analysis indicates that the modified carboxyl groups introduce more interaction types (such as $O_{CO_2}\cdots O_{BDC}$) and quantities, shorten the interaction distance, and enhance the framework-CO_2 interactions. Moreover, multi-carboxyl modification promotes more significant aggregation of guest molecules within the cages, further improving the adsorption capacity. According to the ideal adsorption solution theory (IAST) for pure components, carboxyl-modified MOFs exhibit relatively high selective adsorption performance for carbon dioxide. In the breakthrough experiment, UiO-66-2COOH/AC demonstrated selectivity toward CO_2/N_2 under both dry and wet conditions. Under dry conditions, the penetration time of CO_2 (637 s/g) was much higher than that of N_2 (3.6 s/g); meanwhile, the adsorption capacity reached 8.93 cm^3/g, and the separation coefficient was 55.49. At 50% RH, the penetration time of CO_2 slightly decreased by 3.7% (613 s/g), and the adsorption capacity reduced to 4.04 cm^3/g; the separation coefficient was 49.53, indicating that water molecules competed with CO_2 for adsorption sites, yet the material still maintained significant selectivity.A novel composite aerogel was prepared by loading UiO-66, UiO-66-COOH, and UiO-66-2COOH onto cellulose aerogel using a simple method. The novel composite aerogel has a high specific surface area; the adsorption capacity of CO_2 by UiO-66-2COOH/CA reaches 31.7 cm^3/g at 273K, thereby overcoming the drawback that MOF powder is difficult to process and form. Therefore, our novel cost-effective composite aerogel has great potential for practical CO_2 adsorption applications.

Acknowledgments

The authors are very grateful for financial support from National Natural Science Foundation of China (22376173), Natural Science Foundation of Sichuan Province (2024NSFSC0994), Chengdu Science and Technology Project (2024-YF05-00889-SN), and "the Fundamental Research

Funds for the Central Universities", Southwest Minzu University (ZYN2025012).

Conflict of Interest

There is no conflict of interest.

Supporting Information

Applicable.

References

[1] K. S. Song, P. W. Fritz, A. Coskun, Porous organic polymers for CO_2 capture, separation and conversion, *Chemical Society Reviews*, 2022, **51**, 9831-9852, doi: 10.1039/D2CS00727D.

[2] M. Ding, X. Liu, P. Ma, J. Yao, Porous materials for capture and catalytic conversion of CO_2 at low concentration, *Coordination Chemistry Reviews*, 2022, **465**, 214576, doi: 10.1016/j.ccr.2022.214576.

[3] D. A. Khuong, H. N. Nguyen, T. Tsubota, Activated carbon produced from bamboo and solid residue by CO_2 activation utilized as CO_2 adsorbents, *Biomass and Bioenergy*, 2021, **148**, 106039, doi: 10.1016/j.biombioe.2021.106039.

[4] W. Yu, X. Wu, B. Cheng, T. Tao, X. Min, R. Mi, Z. Huang, M. Fang, Y. Liu, Synthesis and applications of SAPO-34 molecular sieves, *Chemistry,* 2022, **28**, e202102787, doi: 10.1002/chem.202102787.

[5] E. Khoramzadeh, M. Mofarahi, C. H. Lee, Equilibrium adsorption study of CO_2 and N_2 on synthesized zeolites 13X, 4A, 5A, and beta, *Journal of Chemical & Engineering Data*, 2019, **64**, 5648-5664, doi: 10.1021/acs.jced.9b00690.

[6] R. Stanton, D. J. Trivedi, Investigating the increased CO_2 capture performance of amino acid functionalized nanoporous materials from first-principles and grand canonical Monte Carlo simulations, *The Journal of Physical Chemistry Letters*, 2023, **14**, 5069-5076, doi: 10.1021/acs.jpclett.3c00998.

[7] H. Furukawa, K. E. Cordova, M. O'Keeffe, O. M. Yaghi, The chemistry and applications of metal-organic frameworks, *Science*, 2013, **341**, 1230444, doi: 10.1126/science.1230444.

[8] C. Wang, L. Tian, W. Zhu, S. Wang, P. Wang, Y. Liang, W. Zhang, H. Zhao, G. Li, Dye@bio-MOF-1 composite as a dual-emitting platform for enhanced detection of a wide range of explosive molecules, *ACS Applied Materials & Interfaces*, 2017, **9**, 20076-20085, doi: 10.1021/acsami.7b04172.

[9] J. Zheng, L. Sun, C. Jiao, Q. Shao, J. Lin, D. Pan, N. Naik, Z. Guo, Hydrothermally synthesized Ti/Zr bimetallic MOFs derived N self-doped TiO2/ZrO2 composite catalysts with enhanced photocatalytic degradation of methylene blue, *Colloids and Surfaces A: Physicochemical and Engineering Aspects*, 2021, **623**, 126629, doi: 10.1016/j.colsurfa.2021.126629.

[10] H. Wang, W. Shi, L. Hou, G. Li, Z. Zhu, Y. Wang, A cationic MOF with high uptake and selectivity for CO_2 due to multiple CO_2-philic sites, *Chemistry*, 2015, **21**, 16525-16531, doi: 10.1002/chem.201502532.

[11] H. Wan, Y. Que, C. Chen, Z. Wu, Z. Gu, J. Meng, L. Wang, G. Guan, Preparation of metal-organic framework/attapulgite hybrid material for CO_2 capture, *Materials Letters*, 2017, **194**, 107-109, doi: 10.1016/j.matlet.2017.02.033.

[12] M. I. Gonzalez, M. T. Kapelewski, E. D. Bloch, P. J. Milner, D. A. Reed, M. R. Hudson, J. A. Mason, G. Barin, C. M. Brown, J. R. Long, Separation of xylene isomers through multiple metal site interactions in metal-organic frameworks, *Journal of the American Chemical Society*, 2018, **140**, 3412-3422, doi: 10.1021/jacs.7b13825.

[13] M. Drobek, J.-H. Kim, M. Bechelany, C. Vallicari, A. Julbe, S. S. Kim, MOF-based membrane encapsulated ZnO nanowires for enhanced gas sensor selectivity, *ACS Applied Materials & Interfaces*, 2016, **8**, 8323-8328, doi: 10.1021/acsami.5b12062.

[14] A. C. McKinlay, R. E. Morris, P. Horcajada, G. Férey, R. Gref, P. Couvreur, C. Serre, BioMOFs: metal-organic frameworks for biological and medical applications, *Angewandte Chemie (International Ed)*, 2010, **49**, 6260-6266, doi: 10.1002/anie.201000048.

[15] J. Qin, D. Du, W. Li, J. Zhang, S. Li, Z. Su, X. Wang, Q. Xu, K. Shao, Y. Lan, N-rich zeolite-like metal–organic framework with sodalite topology: high CO_2 uptake, selective gas adsorption and efficient drug delivery, *Chemical Science*, 2012, **3**, 2114, doi: 10.1039/c2sc00017b.

[16] H. Wang, L. Hou, Y. Li, C. Jiang, Y. Wang, Z. Zhu, Porous MOF with highly efficient selectivity and chemical conversion for CO_2, *ACS Applied Materials & Interfaces*, 2017, **9**, 17969-17976, doi: 10.1021/acsami.7b03835.

[17] J. Rong, F. Qiu, T. Zhang, Y. Zhu, J. Xu, Q. Guo, X. Peng, Non-noble metal@carbon nanosheet derived from exfoliated MOF crystal as highly reactive and stable heterogeneous catalyst, *Applied Surface Science*, 2018, **447**, 222-234, doi: 10.1016/j.apsusc.2018.03.221.

[18] Y. Li, C. Chen, X. Sun, J. Dou, M. Wei, Metal-organic frameworks at interfaces in dye-sensitized solar cells, *ChemSusChem*, 2014, **7**, 2469-2472, doi: 10.1002/cssc.201402143.

[19] F. Ran, X. Xu, D. Pan, Y. Liu, Y. Bai, L. Shao, Ultrathin 2D metal-organic framework nanosheets in situ interpenetrated by functional CNTs for hybrid energy storage device, *Nano-Micro Letters*, 2020, **12**, 46, doi: 10.1007/s40820-020-0382-x.

[20] H. Furukawa, N. Ko, Y. B. Go, N. Aratani, S. B. Choi, E. Choi, A. O. Yazaydin, R. Q. Snurr, M. O'Keeffe, J. Kim, O. M. Yaghi, Ultrahigh porosity in metal-organic frameworks, *Science*, 2010, **329**, 424-428, doi: 10.1126/science.1192160.

[21] F. Rezaei, S. Lawson, H. Hosseini, H. Thakkar, A. Hajari, S. Monjezi, A. A. Rownaghi, MOF-74 and UTSA-16 film growth on monolithic structures and their CO_2 adsorption performance, *Chemical Engineering Journal*, 2017, **313**, 1346-1353, doi: 10.1016/j.cej.2016.11.058.

[22] X. G. Guo, Z. Zhang, S. Qiu, X. Su, Y. Wang, X. Sun, Versatile tailoring of NH_2-containing metal-organic frameworks with paddle-wheel units, *Chemistry*, 2017, **23**, 17727-17733, doi: 10.1002/chem.201703126.

[23] G. Hao, W. Li, A. Lu, Novel porous solids for carbon dioxide capture, *Journal of Materials Chemistry*, 2011, **21**, 6447-6451, doi: 10.1039/C0JM03564E.

[24] A. R. Millward, O. M. Yaghi, Metal-organic frameworks

with exceptionally high capacity for storage of carbon dioxide at room temperature, *Journal of the American Chemical Society*, 2005, **127**, 17998-17999, doi: 10.1021/ja0570032.

[25] P. L. Llewellyn, S. Bourrelly, C. Serre, A. Vimont, M. Daturi, L. Hamon, G. De Weireld, J. S. Chang, D. Y. Hong, Y. Kyu Hwang, S. Hwa Jhung, G. Férey, High uptakes of CO_2 and CH_4 in mesoporous metal-organic frameworks MIL-100 and MIL-101, *Langmuir*, 2008, **24**, 7245-7250, doi: 10.1021/la800227x.

[26] S. R. Caskey, A. G. Wong-Foy, A. J. Matzger, Dramatic tuning of carbon dioxide uptake *via* metal substitution in a coordination polymer with cylindrical pores, *Journal of the American Chemical Society*, 2008, **130**, 10870-10871, doi: 10.1021/ja8036096.

[27] A. Demessence, D. M. D'Alessandro, M. L. Foo, J. R. Long, Strong CO_2 binding in a water-stable, triazolate-bridged metal-organic framework functionalized with ethylenediamine, *Journal of the American Chemical Society*, 2009, **131**, 8784-8786, doi: 10.1021/ja903411w.

[28] Y. S. Bae, O. K. Farha, J. T. Hupp, R. Q. Snurr, Enhancement of CO_2/N_2 selectivity in a metal-organic framework by cavity modification, *Journal of Materials Chemistry*, 2009, **19**, 2131, doi: 10.1039/b900390h.

[29] X. Zhao, Y. Yuan, P. Li, Z. Song, C. Ma, D. Pan, S. Wu, T. Ding, Z. Guo, N. Wang, A polyether amine modified metal organic framework enhanced the CO_2 adsorption capacity of room temperature porous liquids, *Chemical Communications*, 2019, **55**, 13179-13182, doi: 10.1039/C9CC07243H.

[30] R. Banerjee, H. Furukawa, D. Britt, C. Knobler, M. O'Keeffe, O. M. Yaghi, Control of pore size and functionality in isoreticular zeolitic imidazolate frameworks and their carbon dioxide selective capture properties, *Journal of the American Chemical Society*, 2009, **131**, 3875-3877, doi: 10.1021/ja809459e.

[31] Q. Yang, S. Vaesen, F. Ragon, A. D. Wiersum, D. Wu, A. Lago, T. Devic, C. Martineau, F. Taulelle, P. L. Llewellyn, H. Jobic, C. Zhong, C. Serre, G. De Weireld, G. Maurin, A water stable metal-organic framework with optimal features for CO_2 capture, *Angewandte Chemie (International Ed)*, 2013, **52**, 10316-10320, doi: 10.1002/anie.201302682.

[32] Z. Li, W. Sun, C. Chen, Q. Guo, X. Li, M. Gu, N. Feng, J. Ding, H. Wan, G. Guan, Deep eutectic solvents appended to UiO-66 type metal organic frameworks: Preserved open metal sites and extra adsorption sites for CO_2 capture, *Applied Surface Science*, 2019, **480**, 770-778, doi: 10.1016/j.apsusc.2019.03.030.

[33] J. Fonseca, T. Gong, Fabrication of metal-organic framework architectures with macroscopic size: a review, *Coordination Chemistry Reviews*, 2022, **462**, 214520, doi: 10.1016/j.ccr.2022.214520.

[34] C. Pettinari, R. Pettinari, C. Di Nicola, A. Tombesi, S. Scuri, F. Marchetti, Antimicrobial MOFs, *Coordination Chemistry Reviews*, 2021, **446**, 214121, doi: 10.1016/j.ccr.2021.214121.

[35] N. Hanikel, M. S. Prévot, O. M. Yaghi, MOF water harvesters, *Nature Nanotechnology*, 2020, **15**, 348-355, doi: 10.1038/s41565-020-0673-x.

[36] S. Kumar, S. Jain, M. Nehra, N. Dilbaghi, G. Marrazza, K.-H. Kim, Green synthesis of metal–organic frameworks: a state-of-the-art review of potential environmental and medical applications, *Coordination Chemistry Reviews*, 2020, **420**, 213407, doi: 10.1016/j.ccr.2020.213407.

[37] H. Lin, Y. Yang, Y. C. Hsu, J. Zhang, C. Welton, I. Afolabi, M. Loo, H.-C. Zhou, Metal–organic frameworks for water harvesting and concurrent carbon capture: a review for hygroscopic materials, *Advanced Materials*, 2024, **36**, 2209073, doi: 10.1002/adma.202209073.

[38] G. Liu, T. Chen, J. Xu, G. Li, K. Wang, Solar evaporation for simultaneous steam and power generation, *Journal of Materials Chemistry A*, 2020, **8**, 513-531, doi: 10.1039/C9TA12211G.

[39] S. Sağlam, F. N. Türk, H. Arslanoğlu, Use and applications of metal-organic frameworks (MOF) in dye adsorption: Review, *Journal of Environmental Chemical Engineering*, 2023, **11**, 110568, doi: 10.1016/j.jece.2023.110568.

[40] C. Wang, L. Jia, S. Qin, L. He, Y. Wu, Q. Liu, Y. Jin, Study on the decarbonization mechanism of composite adsorbent by Mg-MOF-74-based modified biochar, *Fuel*, 2024, **357**, 129959, doi: 10.1016/j.fuel.2023.129959.

[41] R. Sakamoto, N. Fukui, H. Maeda, R. Toyoda, S. Takaishi, T. Tanabe, J. Komeda, P. Amo-Ochoa, F. Zamora, H. Nishihara, Layered metal-organic frameworks and metal-organic nanosheets as functional materials, *Coordination Chemistry Reviews*, 2022, **472**, 214787, doi: 10.1016/j.ccr.2022.214787.

[42] R. Fang, A. Dhakshinamoorthy, Y. Li, H. Garcia, Metal organic frameworks for biomass conversion, *Chemical Society Reviews*, 2020, **49**, 3638-3687, doi: 10.1039/D0CS00070A.

[43] M. Nasrollahzadeh, M. Sajjadi, S. Iravani, R. S. Varma, Green-synthesized nanocatalysts and nanomaterials for water treatment: Current challenges and future perspectives, *Journal of Hazardous Materials*, 2021, **401**, 123401, doi: 10.1016/j.jhazmat.2020.123401.

[44] D. Dubbeldam, S. Calero, D. E. Ellis, R. Q. Snurr, RASPA: molecular simulation software for adsorption and diffusion in flexible nanoporous materials, *Molecular Simulation*, 2016, **42**, 81-101, doi: 10.1080/08927022.2015.1010082.

[45] C. J. Casewit, K. S. Colwell, A. K. Rappe, Application of a universal force field to organic molecules, *Journal of the American Chemical Society*, 1992, **114**, 10035-10046, doi: 10.1021/ja00051a041.

[46] M. G. Martin, J. I. Siepmann, Transferable potentials for phase equilibria. 1. united-atom description of *n*-alkanes, *The Journal of Physical Chemistry B*, 1998, **102**, 2569-2577, doi: 10.1021/jp972543+.

[47] A. K. Rappe, C. J. Casewit, K. S. Colwell, I. Goddard, W. M. Skiff, UFF, a full periodic table force field for molecular mechanics and molecular dynamics simulations, *Journal of the American Chemical Society*, 1992, **114**, 10024-10035, doi: 10.1021/ja00051a040.

[48] S. L. Mayo, B. D. Olafson, W. A. Goddard, DREIDING: a generic force field for molecular simulations, *The Journal of Physical Chemistry*, 1990, **94**, 8897-8909, doi: 10.1021/j100389a010.

[49] M. G. Martin, J. I. Siepmann, Transferable potentials for phase equilibria. 1. united-atom description of *n*-alkanes, *The*

Journal of Physical Chemistry B, 1998, **102**, 2569-2577, doi: 10.1021/jp972543+.

[50] S. Kancharlapalli, A. Gopalan, M. Haranczyk, R. Q. Snurr, Fast and accurate machine learning strategy for calculating partial atomic charges in metal-organic frameworks, *Journal of Chemical Theory and Computation*, 2021, **17**, 3052-3064, doi: 10.1021/acs.jctc.0c01229.

Open Access